Development and Numerical Investigation of an Actuator Concept for Shape-Adaptive Airfoil Profile for Horizontal Axis Wind Turbine Rotor

Irfan Ahmed[1]*, Martin Lawerenz[2]

ISROMAC 2016

International Symposium on Transport Phenomena and Dynamics of Rotating Machinery

Hawaii, Honolulu

April 10-15, 2016

Abstract

To cope with the increase in demand on renewable energy, the modern horizontal axis wind turbines have grown in dimension and have already reached a rotor diameter of 150 meter. With the introduction of offshore wind parks, the door to extract multi-megawatt power from wind is opened and has set a trend of continuing increase in wind turbine rotor diameter. This imposes a trade-off between the energy production and the controllability of future wind turbines. The increase in rotor diameter results in higher torque requirement on the active pitch/stall-control motor. Moreover, it is difficult to achieve optimal inflow condition over the entire span length for rigid blades. This results in high structural loading, which in turn reduces the life span of the blades. In light of this situation, smart rotor blades with local airfoil form-adaption promises to be an alternative and effective control scheme for future wind turbines. The authors present the results of investigations on active airfoil form- adaption concept for wind turbine rotor blades. A novel actuator concept is developed for incorporating airfoil trailing edge form-adaption in wind turbine application. Structural analysis of the shape morphing system is carried out and the aerodynamic performance of the shape-adaptive airfoil is presented.

Keywords

Shape-adaptive Airfoil — Actuator Concept — Fluid Structure Interaction

[1]*Department of Thermal Power Engineering, Section of Turbomachinery, University of Kassel, Germany*

[2]*Department of Thermal Power Engineering, Section of Turbomachinery, University of Kassel, Germany*

***Corresponding author**: irfan.ahmed@uni-kassel.de

NOMENCLATURE

α	absolute angle $[rad, °]$
β	relative angle $[rad, °]$
δ	boundary layer thickness $[L]$
δ^*	boundary layer displacement thickness $[L]$
ϵ	modulus of elasticity $[ML^{-1}T^{-2}]$
η	local coordinate of structure mesh $[-]$
ρ	density$[ML^{-3}]$
σ_{eq}	equivalent strength $[ML^{-1}T^{-2}]$
σ_{max}	maximum strength $[ML^{-1}T^{-2}]$
σ_{ts}	ultimate tensile strength $[ML^{-1}T^{-2}]$
σ_y	yield strength $[ML^{-1}T^{-2}]$
θ	boundary layer momentum thickness $[L]$
ξ	local coordinate of structure mesh $[-]$
ζ	local coordinate of structure mesh $[-]$
a	specific work done by an airfoil section $[L^2T^{-1}]$
c	absolute flow velocity $[LT^{-1}]$
c_d	coefficient of drag $[-]$
c_l	coefficient of lift $[-]$
c_p	coefficient of pressure $[-]$
h_k	boundary layer kinematic shape parameter $[-]$
w	relative flow velocity $[LT^{-1}]$
i	incidence angle $[rad, °]$
l	length $[L]$
l_c	chord length $[L]$
l_s	span length $[L]$
p	pressure $[ML^{-1}T^{-2}]$
r	radius $[L]$
t	thickness $[L]$
u	blade speed $[LT^{-1}]$
$D1$	deflection along x axis $[L]$
$D2$	deflection along y axis $[L]$
$D3$	deflection along z axis $[L]$
Ma	Mach number $[-]$
N_f	fatigue life cycle $[-]$
R	stress ratio $[-]$
Re	Reynolds number $[-]$
S_{XX}	normal stress $[ML^{-1}T^{-2}]$
S_{YY}	normal stress $[ML^{-1}T^{-2}]$
S_{ZZ}	normal stress $[ML^{-1}T^{-2}]$
S_{XY}	shear stress $[ML^{-1}T^{-2}]$
S_{YZ}	shear stress $[ML^{-1}T^{-2}]$
S_{ZX}	shear stress $[ML^{-1}T^{-2}]$
$\{f\}$	global force vector $[ML^2T^{-2}]$
$[M]$	global mass matrix $[M]$
$[K]$	global stiffness matrix $[MT^{-2}]$
U	local displacement $[L]$

INDICES

1	leading edge
2	trailing edge
c	circumferential component
s	static quantity

t	total quantity
j	coordinate plane
m	meridian component

ABBREVIATION

CFD	computational fluid dynamics
FSI	fluid structure interaction
PS	pressure side
SS	suction side

INTRODUCTION

Modern wind turbines run mostly at variable rotational speed and use collective pitch control to optimize the energy yield and blade loading. The larger swept area in future wind turbines means the blades would be more susceptive to changing inflow conditions and wind shear. In light of this situation, collective or even individual pitch control alone would not be able to fully tame the radial and azimuthal gradient of the inflow. To compensate, future mega-watt rated wind turbines would require a faster yawing and pitching mechanism which would lead to increased loading on the entire structure. An alternative solution is the introduction of shape-morphing airfoil sections which would allow faster and more detailed flow control over different span-wise locations of the rotor blades.

As the idea of employing shape-adaption technique in wind turbine blades is still in its early stage, the bulk of investigations [19, 21–23, 27] are aimed at understanding the effectiveness and the performance of the flow-control mechanisms for wind turbine applications. The development of dedicated actuator concepts for shape-adaptive wind turbine blades is still in its early stage. A review of the actuator concepts and the state of the art for morphing profiles in wind turbine applications can be found in [24]. Recently [25] have developed pneumatic actuator for wind turbine blade with deflectable flap. [26] developed a pneumatic actuator for flaps to change the airfoil camber. A recent work by [19] describes the advantages in using active flow control techniques in wind turbine applications. Plasma actuators are tested by [27] as active flow-control mechanism for the wind turbines. The results showed an improvement of lift and delay of flow separation for low Reynolds numbered flow. [21] used macro-fiber composite actuators to adapt the airfoil upper surface during operation. [22] have investigated the performance optimization of the thick airfoil used near the rotor hub using various combinations of aerodynamic elements. [23] investigated the use of deformable trailing edge in reducing the blade loading. [28] investigated the concept and material requirement of passive twist for wind turbine blades.

In scope of this investigation, active trailing-edge camber adaption of airfoil is selected as the shape adaption strategy to develop the actuator system. This allows the performance optimization of the airfoil profile for fixed incidence angle as well as performance evaluation of the morphed profile for varying inflow conditions.

1. ACTUATOR CONCEPT

This work focuses on the development of an actuator to actively adapt the shape of the airfoil trailing edge section of horizontal axis wind turbine rotor. In the following sections, the strategy and the design constraints of the shape adaption and the actuation concept are presented.

1.1 Constraints of Shape Adaption

In a first step, a number of criteria is defined for the selection of the actuator for wind turbine application. These boundary conditions are specified by the different aspects of the wind turbine life cycle, spanning from the production process to the aerodynamic and structural performance requirements of the components. The boundary conditions are given in table 1 . These boundary conditions predefine the concept of the shape adaption. The aerodynamic requirements define the shape of the morphed airfoil, whereas the structural requirements define the material of the shape adaptive airfoil section and the actuator system.

Goal	Subtask
Aerodynamic	Increased startup lift
	Controllability of operational loading
	Gradual attaining of stall
	Good post-stall characteristics
Structural	Reduced structural loading
	Increased life cycle
	Reduced weight
Construction	Compatible with existing wind turbine blade structure
	Low complexity of production
Miscellaneous	Ease of Maintenance
	Cost

Table 1. Boundary Conditions for Form-adaptive Wind Turbine Blade Concept.

1.2 Aerodynamic Shape of the Adaptive Airfoil

In the next step, the target slope of the camber line at the trailing edge for the shape-adaptive airfoil is selected. Figure 1 shows schematic of flow-turning over an airfoil along with the velocity and angle definition used in this work. The initial form of the airfoil is depicted in blue and the final bent-shape is shown in green. The Euler

turbine equation states

$$a = (c_{c,2} - c_{c,1})u \tag{1}$$
$$a = (tan\beta_2 - tan\beta_1)c_{m,1}u_1 \tag{2}$$

For a constant-incident flow, the specific work a changes with the change in the angle $\Delta\beta_2$, which corresponds to the change in slope of the camber line at the trailing edge for the shape-adaptive airfoil. The specific work done by a deformed airfoil is given as

$$a^* = (tan\beta_2^* - tan\beta_1)c_{m,1}u_1 \tag{3}$$
$$a^* = (tan(\beta_2 + \Delta\beta_2) - tan\beta_1)c_{m,1}u_1 \tag{4}$$

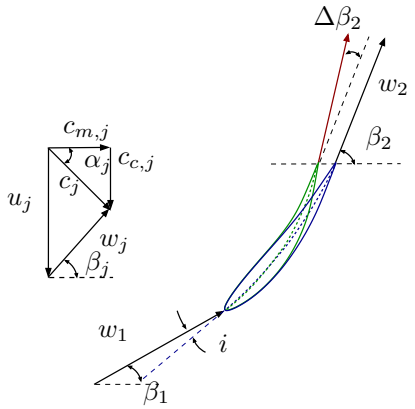

Figure 1. Flow Turning over Shape-Adaptive Airfoil

Hence, a target bending of 8° of the camber line is selected for the implementation in wind turbine application.

1.3 Actuation Concept

The actuation concept for incorporating a bending on the airfoil profile skin is depicted in the figure 2. The underlying concept is to use inward protruding beam elements on the inner side of the airfoil profile skin. The concept is similar to the stringer principal [4]. Bending moment applied on the beams will deform the airfoil skins. The skins of the shape-adaptive airfoil section are modeled to be made of elastic material.

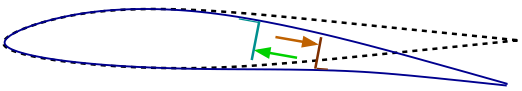

Figure 2. Schematic of Bending of Airfoil Skin

2. METHODICS

In the following sections, the core strategy of the design and analysis of the shape-adaptive airfoil profile are presented.

2.1 FSI Simulation

The interaction of fluid and structure is a considerable phenomenon in wind turbine flow. The modern wind turbine blades with sub 100 m diameter experience substantial loading owing to the aerodynamic forces. The design aspects viz. size, material, inflow velocity, design tip speed ratio, cone angle, control schemes each plays a significant part in the blade loading. The aeroelasticity of the wind turbine blade and tower is acknowledged in the scientific community and design tools are dedicated to model the aeroelastic behavior of the wind turbine flow [8–11].

The majority of these codes resolves the aeroelasticity in a global manner where the basic beam equation is use to model the structure under the aerodynamic loading. From numerical point of view, the modeling of the fluid-structure interaction can be subdivided in the subtasks, a) resolving the fluid field variables, b) resolving the structural response to the body forces acting owing to the fluid flow, c) transferring the deformation of the structural mesh in the fluid model to incorporate the movement of the wetted body. A fully resolved monolithic approach to employ a system of aggregated equations to solve the coupled fluid- structure system for the wind turbine would be numerically challenging and too cumbersome to apply. Recent attempts have been taken by [12] to simulate the fluid structure interaction in a strongly coupled manner. The general trend for turbomachinery is to rather use the staggered approach, i.e. using well established codes for the fluid and the structural solver separately and coupling them at a predefined step. Recently, attempts [13] have been taken to employ the staggered fluid-structure simulation to resolve the wind turbine structural and flow fields.

2.2 Flow Simulation

The flow simulations around the airfoil shapes are carried out with the help of the panel method code XFOIL [1]. The XFOIL code employs linear-vorticity stream function panel method coupled with viscous formulation of the flow-field via integral boundary layer method [2]. The required inputs for the XFOIL code are the airfoil shapes in plain text format and the aerodynamic boundary conditions.

2.3 Structural Simulation

The structural simulation is carried out with the help of the open source software CalculiX [3].
The general equation of motion for the linear static system is as follows [3]

$$[M]\{\ddot{U}\} + [K]\{U\} = \{f\} \tag{5}$$

With

$$\{U\} = U(t) \tag{6}$$
$$\{U(0)\} = U_0 \tag{7}$$
$$\left\{\ddot{U}(0)\right\} = \ddot{U}(0) \tag{8}$$

Here $[M]$ is the global mass matrix, $\{f\}$ is the global force vector, and $[K]$ is the global stiffness matrix. The time derivatives $\dot{U}$ and $\ddot{U}$ of the displacement field U represents the velocity and the displacement of the volume respectively.
The global force vector $\{f\}$ is time-dependent, and contains both inner and outside forces.
The displacement field $\{U\}$ is assumed to be a continuous function of the finite elements in the field, and is described in [3] as

$$U(X) = \sum_{i=1}^{N} \phi_i(\eta, \zeta, \xi)\, U_i \tag{9}$$

The function ϕ_i is the shape function and is defined by the mesh element type. In this case, the 10-node tetrahedral element is used as shown in figure 3.

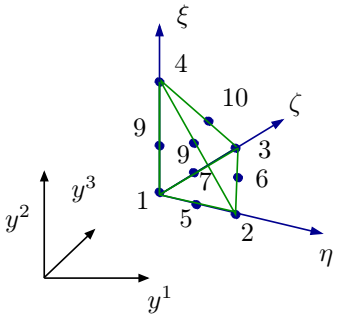

Figure 3. 10-Node Tetrahedral Element C3D10 [3]

2.4 FSI Coupling Scheme

For transient aeroelastic problems, conventional staggered approaches are taken in both serial [5] and parallel modes [6]. Farhat and Lesoinne [7] have recently proposed an improved serial staggered algorithm for time dependent coupled fluid-structure model.

Hence a similar strategy is applied for an assumed steady state behavior. A steady-state staggered fluid-structure interaction scheme is used to numerically simulate the shape-adaptive system. The structural simulation is performed using finite element simulation software CalculiX CrunchiX [3].
Figure 4 depicts the steady-state staggered FSI coupling scheme. At first, the 2D viscous flow field around the airfoil is simulated with the help of XFOIL. In the next step, structural simulation of the morphing structure under aerodynamic and actuation forces is performed using CrunchiX [3]. The deformed shape of the airfoil profile is then used for a second aerodynamic simulation via XFOIL. The resulting aerodynamic forces are then incorporated in further structural simulations to recalculate the required actuation forces.
A parametric study is conducted to determine the shape and the position of the cam profile, the dimensions and relative positions of the beam elements, the required actuation torque, and the material characteristics of the airfoil skin to achieve optimal profile pressure distribution for the morphed airfoil shape.

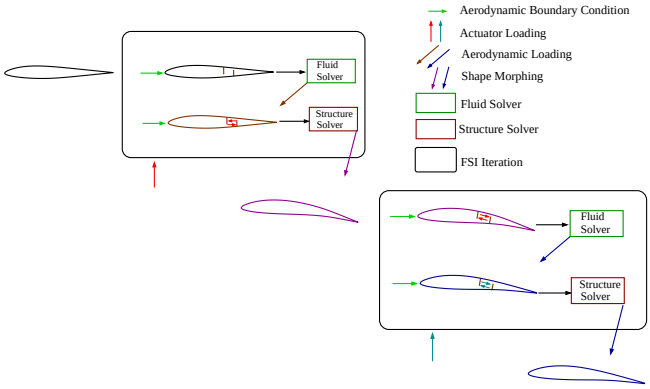

Figure 4. FSI Steady-state Staggered Coupling Scheme

2.5 FSI Coupling Constraints

The numerical scheme presented in this work is based on two dedicated softwares for the simulation of the flow field and the structural response coupled with a mapping algorithm in between the individual software. The mapping algorithm is developed with the assumption of a homogeneous aerodynamic loading along the span-wise direction of the blade element. This is valid in the case of the wind turbine application only when no rotational effect is considered and is similar in strategy to the classical blade element momentum theory [31]. In the actual case, the flow around the wind turbine blade would be 3D in nature and the effects could be incorporated using either 3D Navier-Stokes simulation [32] or from experimental data [33].
If the 3D effects are neglected, the aerodynamic field around the wind turbine blade can be resolved with the help of 2D fluid solver. The structural model, however, requires a 3D representation of the body to calculate the structural response for the given mass and stiffness matrix. Hence a mapping strategy is to be taken to transfer the field variables between the wetted surfaces. The mapping strategy is shown in figure 5. The 2D (z, x) fluid mesh is assumed to be symmetric in y direction. The aerodynamic pressure distribution is thus mirrored along the y axis. The aerodynamic loads are interpolated over (z, x), and transferred to the free surface of the 3D (y^1, y^2, y^3) structure mesh. A spline inter-

polation scheme is used to interpolate the aerodynamic forces on the nodes of the C3D10 tetrahedral elements.

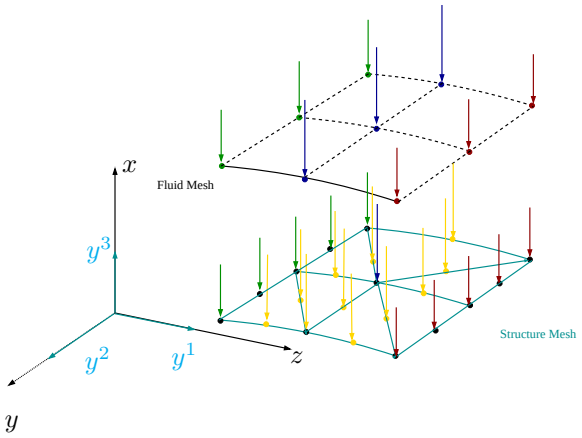

Figure 5. FSI Mapping Scheme

A similar strategy is adopted for the coupling of the displacement matrix of the structure mesh to the fluid mesh. Hence the displacement field of the nodal elements of the structural mesh are translated to the deformed shape of the aerodynamic body. The mesh of the aerodynamic solver is then updated and the respective sweep of aerodynamic simulation is carried out.
Benchmark tests of the flow solver XFOIL [30] and of the structural solver CalculiX CrunchiX [29] are available and show reliable performance. To validate the predictions made by the individual softwares, actual experimental investigations are required on prototype blade section.

3. NUMERICAL SIMULATION

The boundary conditions, preparations and execution of the numerical simulations are presented in the following sections.

3.1 Geometry and Boundary Condition

For the numerical simulation the following geometric and boundary conditions are applied.
Figure 6 depicts the base geometry of the shape-adaptive airfoil. The aerodynamic shape of the base airfoil is taken to be that of a NACA 0012 airfoil. The chord length of the airfoil is $l_c = 200$ mm, the span length is $l_s = 198$ mm. The airfoil is divided into two distinctive parts, the first 40% of the chord length is modeled as to be rigid, and the later 60% of the chord length is modeled to be shape adaptive. The shape adaptive part is divided into two slender beam sections forming the respective surface profiles of the upper and lower surfaces of NACA 0012 airfoil. The thickness of the beam elements are taken as to be $t = 2$ mm. To provide for the transfer of the actuator forces, two inward protruding beam sections each of 3 mm thickness are incorporated in the adaptive sections of the airfoil. The distance of the upper and lower inward-protruding beam sections from the fixed part are $l_{upper} = 22$ mm and $l_{lower} = 37$ mm respectively. The heights of the beams are $h_{upper} = 14$ mm, and $h_{lower} = 8.7$ mm respectively.

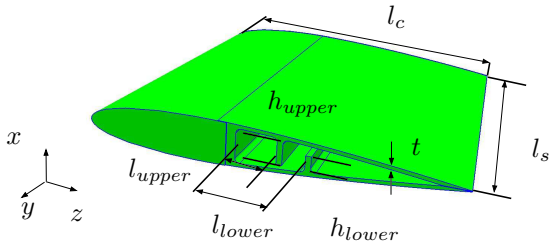

Figure 6. Base Geometry of Shape-Adaptive Airfoil

For the structural simulation, the elements pertaining to the leading edge section of the airfoil are defined with single point constraints boundary condition having zero degree of freedom. The front end sections of the shape-adaptive airfoil are modeled as fixed with the leading edge of the airfoil. The material is defined as isotropic in nature and respective modulus of elasticity, density and Poisson's ratio are defined. The governing equations are solved for static analysis of a linear-elastic system. The aerodynamic and the actuator loadings are provided as distributed pressure loadings on the element faces of the respective surfaces.
The boundary conditions for the flow simulations are selected as Reynolds number $Re = 986557.29$ and Mach number $Ma = 0.209$ corresponding to a relative inflow velocity of $w_1 = 70.71$ m/s.

3.2 Discretization of the Aerodynamic Flow-field

The discretization of the airfoil for the aerodynamic flow simulation is directly related to the airfoil profile coordinate point distribution. Hence, numerical routine is used to generate the base airfoil and the deformed airfoil shapes. The deformation of the shape-adaptive airfoil is obtained from the CalculiX CrunchiX simulation result and is updated for subsequent aerodynamic simulation. Batch scripts are prepared to load the deformed airfoil profile in XFOIL and the geometric design routine of XFOIL is used to check and smooth the paneling of the airfoil profile. The airfoils are discretized in 226 panels.

3.3 Discretization of the Structure

The structural mesh is generated with the help of open source mesh generation software NETGEN [14,15]. The CAD model of a blade section is loaded in NETGEN as step (ISO 10103) format. The blade-geometry contains filleted surface to eliminate structurally weak sections. In a first step, the geometric model is loaded in the NETGEN software and analyzed for topological failure and healed if any found. Through a selection of parameters,

the mesh granularity, local and global mesh-size grading, discretization of curved geometry and the number of surface and volume mesh optimization are set, and the final volume mesh is generated. The software automatically detects the edges present in the CAD model and divides the 3D mesh in several faces, with a boundary number assigned to each face. This information is used for later definition of the boundary conditions in the structural solver. The automatic mesh generator discretizes the geometry in 183451 nodal elements. A total of 57360 surface elements and 92510 volume elements are constructed from these nodal points.

3.4 FSI Sweep

In the first step, Python routine is used to generate the CalculiX GraphiX batch data to (*.fbl) to read the mesh generated by NETGEN and save the volume and surface meshes for the structural simulation.
In the following step, the CalculiX GraphiX routine is run in batch mode and the element and node indices along with the boundary condition files are saved.
Numerical routines using the open source software GNU Octave are developed to read the CalculiX GraphiX output file and the aerodynamic loading files obtained from the XFOIL simulation result.
In the next step, the FSI mapping algorithm is implemented and the input files for the structural solver CalculiX CrunchiX are prepared.
In the following step, GNU Octave codes for interpreting the deformed shape of the structure are run and the deformed airfoil shape is passed to the XFOIL code for aerodynamic simulation.

4. RESULTS

In the following sections the results of the FSI simulations are presented.

4.1 FSI Simulation First Sweep

The first FSI sweep starts with the aerodynamic flow simulation of the base airfoil with XFOIL. The resulting aerodynamic loadings are used for the structural solver. The actuator forces required for deforming the base airfoil with the target deformation angle are obtained via repeated iterations of the structural simulation.

4.1.1 XFOIL Simulation of Base airfoil

In a first step, the NACA 0012 airfoil is simulated for an incidence angle $i = 0°$. The resulting pressure distribution around the airfoil surface profile is depicted in figure 7. For the symmetric airfoil with 0° incidence angle, the aerodynamic loadings are identical for the upper and lower surfaces of the airfoil.

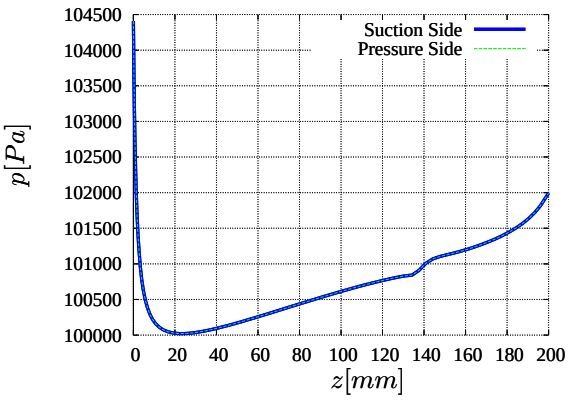

Figure 7. Surface Pressure Distribution for Base Airfoil

4.1.2 CalculiX Simulation

In the next step, the FSI coupling routine is implemented, first by reading the volume and surface meshes generated by the CalculiX GraphiX software. The aerodynamic loadings are fetched from the XFOIL simulation result of the base airfoil. Actuator forces are defined in the CalculiX CrunchiX input file, and structural simulations are carried out to determine the actuator loads for achieving the target bending of the airfoil. The structural simulations are carried out for static analysis with the help of SPOOLES solver [16].
The resulting deflection of the airfoil profile are depicted in figure 8. The deflection $D1$ and $D3$ are along the airfoil thickness and chord directions respectively. The trailing edge of the airfoil is deflected by $D1 = 28mm$. The inward-protruding beam elements are rotated in the $x-z$ plane owing to the bending of the airfoil upper and lower surfaces. These rotation is translated in a maximum shift of $D3 = -4.34$ mm for the upper inward-protruding beam, and that of $D3 = 3.21$ mm for the lower inward-protruding beam.

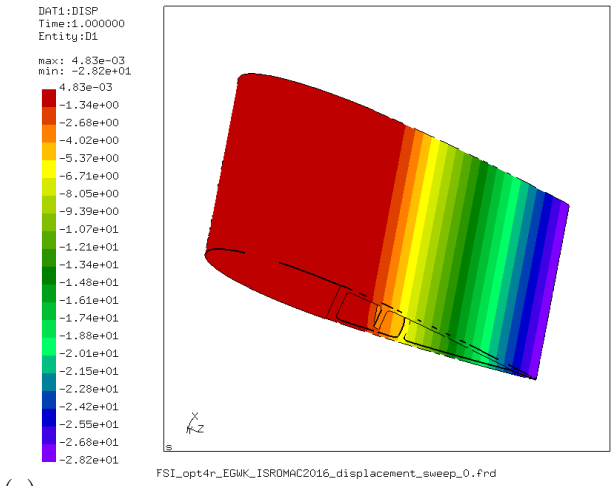

(a)

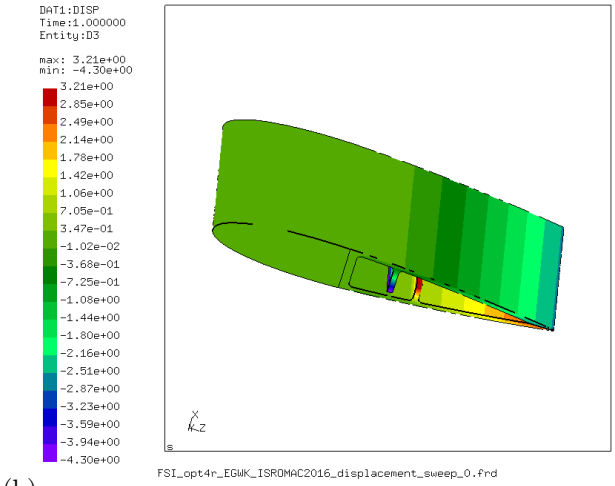

(b)

Figure 8. CalculiX: Deformations (a) $D1$ (b) $D3$

4.1.3 Resulting Airfoil Shape

The resulting airfoil shape after the first FSI sweep is shown in figure 9. The camber line of the shape-adaptive airfoil is deformed by 8° total, which translates to a bending of about 28 mm at the trailing edge.

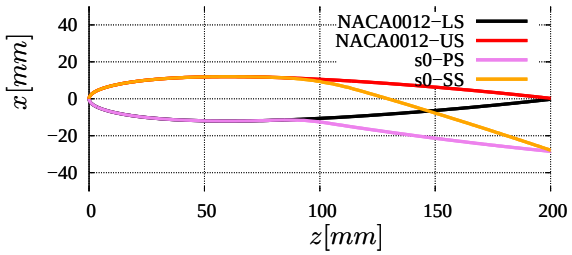

Figure 9. Shape-adapted Airfoil with Base Airfoil Profile

4.2 FSI Simulation Second Sweep

In the second FSI sweep, the aerodynamic loading on the airfoil is updated from the aerodynamic simulation result from XFOIL. The actuator forces are kept unchanged to those of the first FSI sweep.

4.2.1 XFOIL Simulation of Shape-Adapted Airfoil

The aerodynamic loading from the XFOIL simulation for the shape-adapted airfoil is presented in figure 10. The pressure distributions show rough profile which result from the waviness in the airfoil panels. This is a direct result of the mapping algorithm for the FSI simulations.

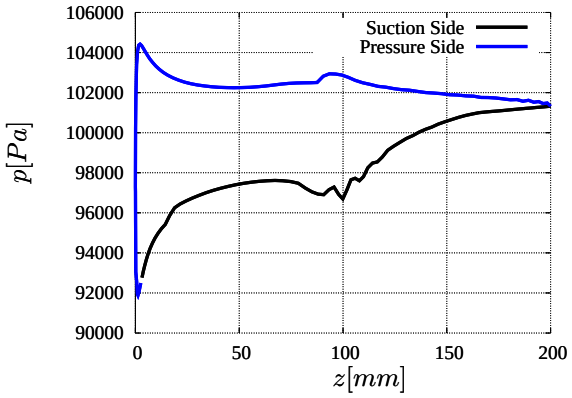

Figure 10. Updated Aerodynamic Loading

4.2.2 CalculiX Simulation with Recalculated Aerodynamic Forces

In the next step, structural simulation are carried out with the updated aerodynamic loadings. The actuator forces are kept unchanged for this stage to investigate

the effect of the changed aerodynamic loadings on the deformation of the airfoil surfaces.

4.2.3 Resulting Airfoil Shape

The resulting shape after the second sweep are shown in figure 11. The shapes of the airfoil profile are changed owing to the updated aerodynamic loadings. The pressure side has a total of 1.12 mm less deflection and the suction side has 0.36 mm more deflection at the trailing edge. The difference in the deflections are 0.56% and 0.18% of the chord length respectively.

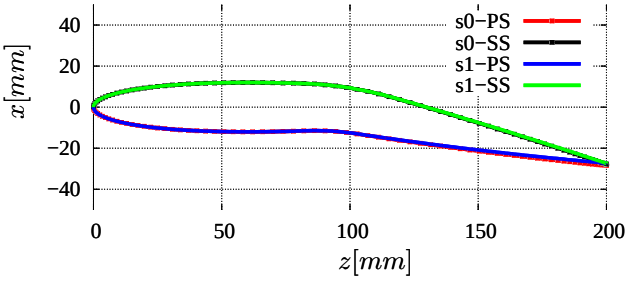

Figure 11. Shape-adapted Airfoils for Subsequent FSI Sweeps

4.2.4 CalculiX Simulation with Recalculated Actuator Forces

In the next step, structural simulations are carried out with varying actuator forces to achieve the target camber deformation of the airfoil. Hence 6 further iterations are carried out to obtain the end result. The resulting trailing edge deflection for the airfoil upper and lower surfaces are shown in figure 12. the The final actuator forces on the upper and lower beam sections are increased 4.23% and 1.51% respectively to achieve the camber line bending of 8°.

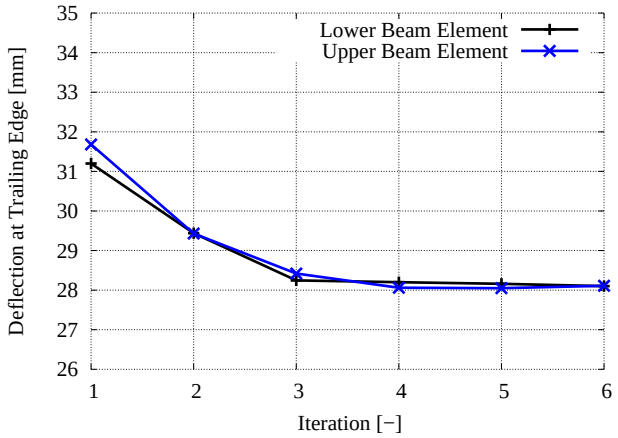

Figure 12. Iterations of Sweep 2

4.3 Aerodynamic Analysis

In the following step, the aerodynamic analysis of the shape adapted airfoil is carried out. The shape-adapted airfoil has a lift coefficient of $c_l = 1.2867$ and a drag coefficient of $c_d = 0.02128$.

The airfoil profile coefficient of pressure distributions are depicted in figure 13. Results of the first FSI sweep and those of the final FSI sweep are presented along with the coefficient of pressure distribution for the symmetric NACA 0012 airfoil. The rough distribution of the c_p values are observed at sections where the deformed airfoil profile shows wavy nature. The cause of this lies on small changes in deflection values interpolated by the FSI mapping algorithm.

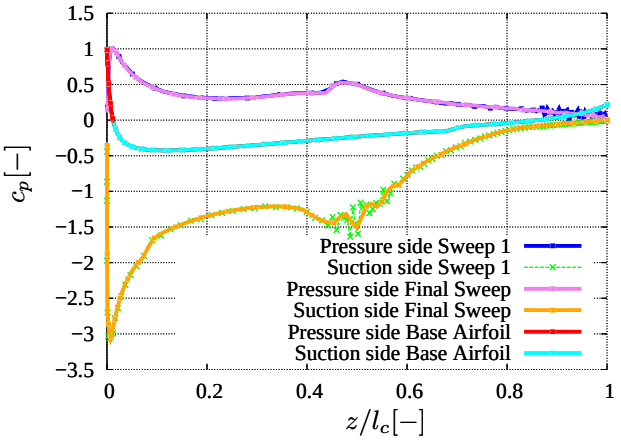

Figure 13. Airfoil Profile Coefficient of Pressure Distributions

The kinematic shape parameter over the airfoil profiles are shown in figure 14. Interestingly the values of h_k for both shape adapted airfoil differ from that of the base NACA 0012 airfoil in the fixed section upstream to the shape-adaptive section. Whereas the change in

the pressure side occur close to the shape-adaptive section, the suction side distributions of h_k exhibit an early peak near the nose section. For the shape-adaptive airfoils from both FSI sweeps, distinctive jump in h_k is observed upstream of the shape-adaptive section. The values of h_k reach 9 for both the cases. An investigation of the boundary layer shows, however, no trace of flow separation.

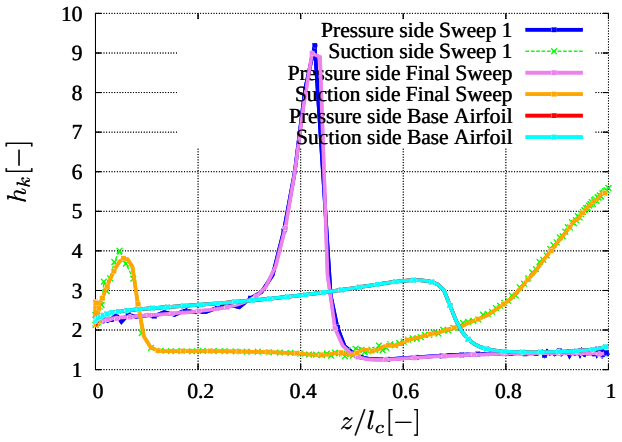

Figure 14. Airfoil Profile Kinematic Shape Parameter Distributions

The boundary layer displacement thickness over the airfoil profiles are shown in figure 15. Also in this case, a shift in the change in boundary layer upstream of the shape-adaptive sections are observed for the pressure sides of the shape-adaptive airfoil. For the suction side, the values of δ^* increase starting from the shape-adaptive section.

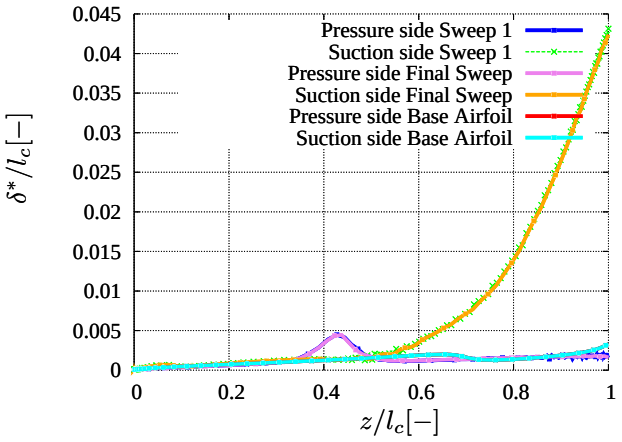

Figure 15. Airfoil Profile Boundary Layer Displacement Thickness Distributions

The boundary layer momentum thickness over the airfoil profiles are shown in figure 16. For the shape-adaptive airfoils, the suction side boundary layer momentum thickness θ increases way upstream of the shape-adaptive section. This, in combination of the relatively unchanged boundary layer displacement thickness distribution (figure 15) results in the difference in the suction side kinematic shape factor change relative to the NACA 0012 airfoil observed in (figure 14). Also noticeable is the change of the boundary layer momentum thickness distribution for the pressure sides upstream of the shape-adaptive sections. Comparing the onset of these changes to those of the boundary layer displacement thickness (figure 15), the shift of the kinematic shape factors in (figure 14) for the pressure sides are explained.

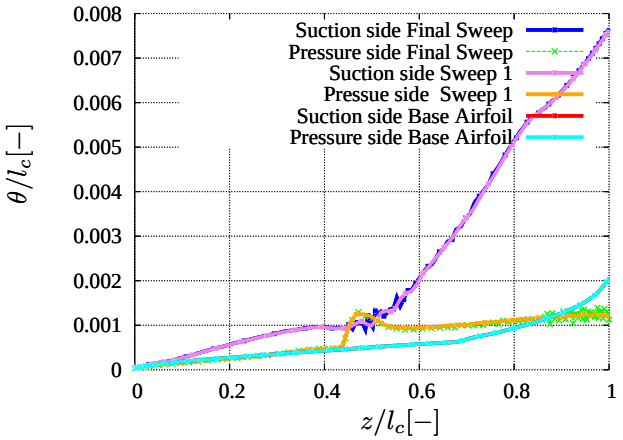

Figure 16. Airfoil Profile Boundary Layer Momentum Thickness Distributions

4.4 Structural Analysis

The resulting shape-adapted airfoil is then analyzed for structural properties. The material of the airfoil is taken as Aluminium alloy (EN AW 2024-T4 [AlCu4Mg1]). The alloy has a density of $\rho = 2.77$ g/cm^3 an ultimate tensile strength $\sigma_{ts} = 469$ MPa, yield strength of $\sigma_y = 324$ MPa, and a modulus of elasticity of $\epsilon = 73.1$ GPa [17].

In a first step, stress distributions are investigated to check for design weak points. The principal stresses of the shape-adapted airfoil are presented in figure 17. The principal stress along x axis is presented in figure 17 (a). The bases of the upper and lower inward-protruding beams undergo the maximum stresses in this direction. The values remain within the safety limit for the given material. Figure 17 (b) depicts the principal stress along y axis. Although the value remains within the safety limit, the presence of stresses along y direction suggests compound bending of the airfoil surfaces along the spanwise direction. Figure 17 (c) depicts the principal stress

along z axis. The material is stressed at the most along the z direction owing to the tensile and compressive loads from the shape adaption. The critical areas are the sections from the beginning of the shape-adaptive part to the inward-protruding beam sections where the actuator loads are applied. The upper section of the shape-adaptive part of the airfoil undergoes the highest stress. Results from initial design iterations suggest that, a shift in the position of the inward-protruding beams further towards the trailing edge would improve the situation. Hence the positioning of beams are selected at the furthest possible station for the current airfoil dimension.

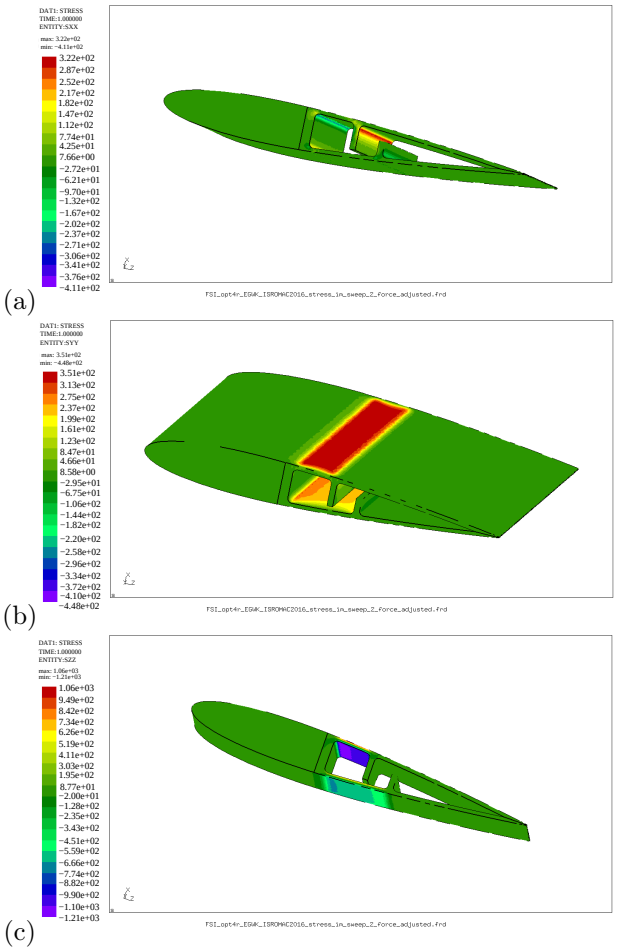

Figure 17. CalculiX: Distributions of Principal Stresses (a) S_{XX} (b)S_{YY} (c)S_{ZZ}

In the next step, the von Mises stress distribution is observed and is depicted in figure 18. The highest von Mises stress is observed in the suction side near the beginning of the shape-adaptive part of the airfoil. However, with a maximum value of 106 $\mathrm{N/mm^2}$ the stresses remain well within the safety region of the selected material.

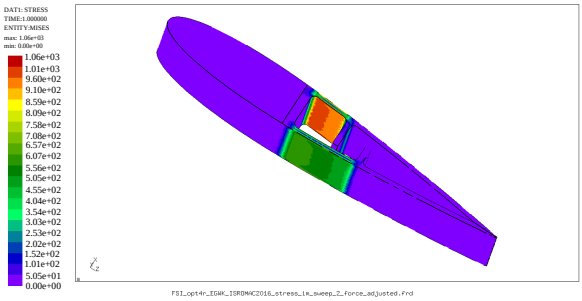

Figure 18. CalculiX: von Mises Stress Distributions

4.4.1 Fatigue Analysis

In order to check the feasibility of the proposed design, the system should be checked for the fatigue loading. In this section, the system is checked for the stresses resulting from the shape deformation. The following assumptions and boundary conditions are considered for the prediction of the fatigue life cycle for the adaptive system. The loading is taken to be unidirectional with a stress ratio $R = 0$, the maximum stress is taken to be of the von Mises stress calculated by the structural solver $\sigma_{max} = 106$ MPa. Now from empirical database presented in [18] the fatigue life cycle can be predicted for the fatigue stress with the help of the following equations

$$\sigma_{eq} = \sigma_{max} \left(1 - R\right)^{0.52} \tag{10}$$

$$logN_f = 20.83 - 9.09log(\sigma_{eq}) \tag{11}$$

It is to be noted that the equations are given for stresses in kilopound per square inch (ksi) [18]. The resulting fatigue life cycle is $N_f = 10^{10}$. Hence it is to be noted that in the actual case, the stress ratio would take a positive value and the fatigue life cycle would increase. The choice of $R = 0$ is here appropriate as the zero deformation load of the wind turbine blade life cycle is an unknown value at this moment.

5. DESIGN

The deflection $D3$ from the the beam elements give a pretext for the design of the actuation system. The actuator is modeled as a kinematic module able to rotate around its axis and has a cam profile which determines the actuation forces exerted on the different beam sections. The actuation force is achieved through implementing a torque which translates in a coupled bending moment on the profile upper and lower skins.

6. DESIGN OF THE CAM PROFILE

The design of the cam profile for the actuation is shown in figure 19. In this case a double cam profile is used to simultaneously exert the actuating forces on the upper

and lower protruding beam elements. The dimensions of the cam profile are taken to incorporate the required bending shape of the airfoil. Hence, the deflections $D3$ of the upper and lower beams have to be realized by actuating the cam profile. The cam is designed to have a base diameter of $d_b = 12$ mm. The upper and lower eccentricity are taken as $l_1 = 3$ mm and $l_2 = 2$ mm respectively. These values correspond to the deflection $D3$ of the beams at the mid-plane. The cam has to be rotated counter-clockwise to achieve the required shape adaption of the base airfoil. A gradual slope is incorporated to hinder sudden shape change. The values of the angles are selected as $\gamma_1 = 62°$, $\gamma_2 = 114°$,$\gamma_3 = 74°$ and $\gamma_4 = 110°$. The material for the cam is taken as stainless steel (DIN X2CrNiMoCuWN25-7-4).

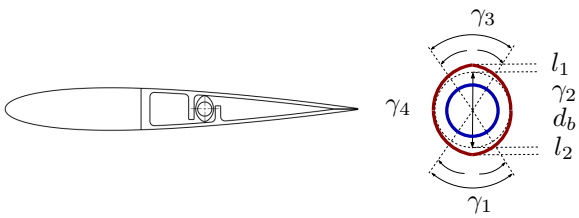

Figure 19. Design of the Cam Profile

7. SUMMARY

In scope of this work, multidisciplinary design strategy of shape-adaptive airfoil for wind turbine application is presented. A low order fluid structure interaction strategy is developed and implemented for a design case scenario for actively adaptive airfoil profile. This strategy allows one to plan, design and pre-investigate potential design-flaws with very little effort. A design scenario is presented and detailed aerodynamic and structural characteristics are investigated for the prototype. A novel actuation system is proposed to implement in airfoil shape adaption.

The FSI mapping algorithm should be extended to incorporate 3D mapping. This would allow one to investigate the effect of 3D aerodynamic phenomenon on the structural response and vice versa. The initial design does not consider the unsteady nature of the fluid structure interaction. For the further design of the cam profile, the unsteady effect of the shape change has to be incorporated. For that purpose, the flow field has to be resolved for unsteady effects. Hence it calls for the inclusion of CFD simulation of the flow field around the airfoil shape and detailed experimental investigations of the aerodynamic and structural behaviors.

8. ACKNOWLEDGMENTS

The authors would like to acknowledge Mr. Mark Drela for his airfoil panel method code XFOIL, Mr. Guido Dhondt and Mr. Klaus Wittig for the structural solver CalculiX, and Mr. Jochaim Schöberl for his mesh generation software NETGEN.

REFERENCES

[1] Mark Drela (1989). An analysis and design system for low Reynolds number airfoils.

[2] Mark Drela and Michael B. Giles (1987). Viscous-inviscid analysis of transonic and low Reynolds number airfoils. AIAA Journal, 25(10):1347–1355.

[3] Guido Dhondt (2004). The Finite Element Method for Three-Dimensional Thermomechanical Applications. John Wiley & Sons, Ltd. ISBN: 0-470-85752-8.

[4] Hans Peter Monner (2000). Erzielung einer optimierten Tragflügelverwolbung durch den Einsatz formvariabler Klappenstrukturen. DLR-Forschungsbericht. 2000-30, Institut für Strukturmechanik, Braunschweig.

[5] John T. Batina (1990). Unsteady Euler Airfoil Solutions Using Unstructured Dynamic Meshes. AIAA Journal, 28(2):1381–1388.

[6] Sisira Weeratunga and Eddy Pramono (1994). Direct Coupled Aeroelastic Analysis Through Concurrent Implicit Time Integration on a Parallel Computer. AIAA-94-1550-CP.

[7] C. Farhat and M. Lesoinne (2000). Two Efficient Staggered Algorithms for the Serial and Parallel Solution of Three-Dimensional Nonlinear Transient Aeroelastic Problems. Computer Methods in Applied Mechanics and Engineering, 182(3–4):499–515.

[8] David A. Simms, S. Schreck, M. Hand and L. J. Fingersh (2001). NREL unsteady aerodynamics experiment in the NASA-Ames wind tunnel: a comparison of predictions to measurements. National Renewable Energy Laboratory Golden, CO, USA.

[9] Flemming Rasmussen, Morten Hartvig Hansen, Kenneth Thomsen, Torben Juul Larsen, Franck Bertagnolio, Jeppe Johansen, Helge Aagaard Madsen, Christian Bak and Anders Melchior Hansen (2003). Present status of aeroelasticity of wind turbines. Wind Energy, 6(3):213–228.

[10] Martin Otto Laver Hansen, Jens Nørkær Sørensen, S. Voutsinas, Niels Sørensen and H. A. Madsen (2006). State of the art in wind turbine aerodynamics and aeroelasticity. Progress in Aerospace Sciences, 42(4):285–330.

[11] M. H. Hansen (2004). Aeroelastic stability analysis of wind turbines using an eigenvalue approach. Wind Energy, 7(2):133–143.

[12] Ouahiba Guerri (2009). Fluid structure interaction of a parked wind turbine airfoil. 18 ème Congrès Français de Mécanique, Marseille, 24-26.

[13] Ivan Dobrev and Fawaz Massouh (2007). Fluid-structure interaction in the case of a wind turbine rotor. 18 ème Congrès Français de Mécanique, Grenoble, 27-31.

[14] J. Schöberl (2003). Netgen 4.3.

[15] J. Schöberl (1997). NETGEN - An advancing Front 2D/3D-Mesh Generator based on Abstract Rules. Computing and Visualization in Science, 1:41–52.

[16] C. Ashcraft, R. G. Grimes, D. J. Pierce and D. K. Wah (1999). The User Manual for SPOOLES, Release 2.2: An Object Oriented Software Library for Solving Sparse Linear Systems of Equations. Boeing Shared Services Group, P.O Box 24346, Mail Stop 7L-22, Seattle, Washington 98124 USA. http://netlib.bell-labs.com/netlib/linalg/spooles/spooles.2.2.html.

[17] Werner Hesse (2006) Aluminium-Schlüssel:= Key to aluminium alloys 7. Aufl. http://hds.hebis.de/ubks/Record/HEB183174593. ISBN 9783870172824. Aluminium-Verl. Düsseldorf.

[18] Department of Defense Handbook: Metallic Materials and Elements for Aerospace Vehicle Structures MIL-HDBK-5J. 31 January 2003. United States Department of Defense.

[19] Guannan Wang, Jakub Walczak, Basman Elhadidi, Mark Glauser and Hiroshi Higuchi (2011). Preliminary Investigation of the Active Flow Control Benefits on Wind Turbine Blades. 6th AIAA Theoretical Fluid Mechanics Conference (3611). http://arc.aiaa.org/doi/pdf/10.2514/6.2011-3611.

[20] Justin Meijerink and Harry Hoeijmakers (2011). Plasma Actuators for Active Flow Control on Wind Turbine Blades. 29th AIAA Applied Aerodynamics Conference. http://arc.aiaa.org/doi/pdf/10.2514/6.2011-3353.

[21] Marco Debiasi, Yann Bouremel, H. H. Khoo, S. C. Luo, and E. Z. Tan (2011). Shape Change of the Upper Surface of an Airfoil by Macro Fiber Composite Actuators. 29th AIAA Applied Aerodynamics Conference. http://arc.aiaa.org/doi/pdf/10.2514/6.2011-3809.

[22] Adam M. Ragheb and Michael S. Selig (2011). Multi-Element Airfoil Configurations for Wind Turbines. 29th AIAA Applied Aerodynamics Conference. http://arc.aiaa.org/doi/pdf/10.2514/6.2011-3971.

[23] Peter Bjørn Andersen (2010). Advanced Load Alleviation for Wind Turbines using Adaptive Trailing Edge Flaps: Sensoring and Control. Risø-PhD-61(EN). ISBN 978-87-550-3824-0.

[24] T. Barlas, J. W. van Wingerden, A. Hulskamp and G. van Kuik (2008). Closed-loop Control Wind Tunnel Tests on an Adaptive Wind Turbine Blade for Load Reduction. Proceedings of the 46th AIAA/ASME. http://arc.aiaa.org/doi/pdf/10.2514/6.2008-1318.

[25] Christian Meldgaard and Michael Friedrick (2012). Wind Turbine Blade With Deflectable Flaps. United States Patent 8087889 B2.

[26] Anders Rebsdorf, Michael Friedrich and Christian Meldgaard (2009). Wind Turbine Blades with Cambering Flaps. European Patent EP2019203A2.

[27] Harry Hoeijmakers and Justin Meijerink (2011). Plasma Actuators for Active Flow Control on Wind Turbine Blades.

[28] Mike Zuteck (2002). Adaptive Blade Concept Assessment: Curved Planform Induced Twist Investigation. Sandia National Laboratories. http://windpower.sandia.gov/other/022996.pdf.

[29] Andrea Starnini (2013). Calculix-Theory benchmarks: linear elastic. http://starnini.altervista.org/FEMcomp.html.

[30] Michael S. Selig (2003). Low Reynolds Number Airfoil Design Lecture Notes. VKI Lecture Series. Applied Vehicle Technology (AVT) Panel. NATO Research and Technology Organization (RTO).

[31] Emrah Kulunk (2011). Aerodynamics of Wind Turbines, Fundamental and Advanced Topics in Wind Power. ISBN 978-953-307-508-2. InTech. http://www.intechopen.com/books/fundamental-and-advanced-topics-in-wind-power/aerodynamics-of-windturbines.

[32] Iván Herráez, Bernhard Stoevesandt, and Joachim Peinke (2014). Insight into Rotational Effects on aWind Turbine Blade Using Navier–Stokes Computations. Energies 2014, 7, 6798-6822; doi:10.3390/en7106798. ISSN 1996-1073.

[33] Christian Bak, Jeppe Johansen, Peter B. Andersen (2006). Three-Dimensional Corrections of Airfoil Characteristics Based on Pressure Distributions. European Wind Energy Conference and Exhibition (EWEC), 27. Feb. – 2. Mar. 2006, Athens, Greece.